An Inverse Thermal Modeling Approach for Thermal Parameter and Loss Identification in an Axial Flux Permanent Magnet Machine

Hendrik Vansompel, Anna Yarantseva, Peter Sergeant, and Guillaume Crevecoeur

***Abstract*—Despite the use of state-of-the-art thermal modeling tools in the design stage, the measured thermal behavior of prototype electrical machines can differ significantly from the modeled ones. This paper shows how a thermal model, based on finite element method, of an electric machine can be improved using inverse modeling techniques. In a thorough study, a forward high fidelity finite element thermal model of a 4 kW axial flux PM machine is introduced and improved using inverse modeling techniques via non-collocated thermal sensors. Parametric model order reduction of the high fidelity finite element thermal model based on moment matching method is performed to make the recovery of the actual thermal parameters characterizing the thermal behavior of the axial flux PM machine tractable. Additionally, the same reduced order model is used to identify the different power loss components in the machine. Experimental results confirm that the presented two-stage approach is capable to identify the thermal parameters and losses with high accuracy.**

***Index Terms*—Thermal sensors, Loss measurement, Inverse problems, Reduced order systems**

NOMENCLATURE

ρ	Mass density.
C_{p}	Specific heat capacity.
k	Thermal conductivity.
h	Convective heat flux coefficient.
Q	Volumetric loss density.
$\cdot_{\mathrm{ep}}$	Epoxy resin parameter.
$\cdot_{\mathrm{cu}}$	Copper parameter.
$\cdot_{\mathrm{wi}}$	Winding parameter.
f_{wi}	Winding filling factor.

I. INTRODUCTION

OPTIMAL motor performance is a result of a multiphysics design process including electromagnetic, thermal and mechanical aspects [1]–[4]. Proper thermal design of an electric machine ensures that the cooling provisions are capable to handle the maximum continuous rating. Generally, the maximum continuous rating is determined by thermal constraints rather than by electromagnetic ones [5]. From efficiency point of view, proper thermal design includes effective cooling of the motor winding as the resistivity of the copper windings increases with temperature. Excessive temperatures or hot spots are harmful for the winding insulation [6], [7] or can irreversibly demagnetize permanent magnets [3]. On the other hand proper thermal design is necessary to avoid excessive safety margins. This becomes particularly important in size and weight critical applications such as electric mobility applications [8] . Improving the thermal design of an existing electromagnetic design is used to decrease the motor size, achieve higher output power for a given motor size, and extend the motor operational life [9]. Therefore, high fidelity thermal models are necessary for safe operation safeguarding maximum efficiency.

High fidelity thermal models generally combine a finite element thermal model with computational fluid dynamics for the convective heat flux in the air gap and at the machine outer boundaries [4], [10], [11]. Despite the high level of modeling details, discrepancies between modeled and measured temperatures are still observed [12].

Common elements to explain these differences are numerous [13]. Even in finite element modeling, the level of detail is not up to the level of the different strands in the winding. In many cases this even does not make sense since the individual strands are distributed randomly when pressing the strands into the slots [14]. Therefore, these finite element models use homogenization techniques to approximate the strongly anisotropic thermal conductivities of the motor windings in the different directions [15]. Also the thermal contact resistance at boundaries between different materials [14], [16], [17] is indicated as a cause of modeling inaccuracies. Other authors [18] observe a high impact of process parameters, *e.g.* injection pressure used in the infiltration of the stator windings with potting compound. Although these indicated possible causes of temperature discrepancies, none has tried to correct their thermal model making use of the temperature measurements subsequently resulting in a thermal model with improved accuracy.

Next to the accuracy of the thermal model itself, differences in modeled and measured temperatures are very often caused by power losses which are different than the estimated ones. Even if a direct loss measurement, *i.e.* power balance

Manuscript received December 8, 2017; revised January 29, 2018 and March 24, 2018; accepted April 26, 2018.

The authors are with the Electrical Energy Laboratory, Department of Electrical Energy, Metals, Mechanical Constructions and Systems, Ghent University, 9000 Ghent, Belgium, and also with Flanders Make, 3920 Lommel, Belgium (e-mail: Hendrik.Vansompel@UGent.be; Anna.Yarantseva@UGent.be; Peter.Sergeant@UGent.be; Guillaume.Crevecoeur@UGent.be).

Color versions of one or more of the figures in this paper are available online at http://ieeexplore.ieee.org.

monitoring, is done, the subdivision of the total measured loss over the different power loss components in the machine remains uncertain. Very often iron losses are indicated as underestimated in the design phase, as effects such as the cutting process, mechanical stress, welding, *etc*. [19], [20] during the manufacturing processes are known to increase the iron losses significantly.

An approach to separate the different loss components in electric machines is introduced by [21]. In this combined experimental and numerical approach, different sets of direct measurements of the total losses are compared to modeled ones until the best fit is found.

This work aims at improving the accuracy of a high fidelity thermal finite element model in a first stage by identifying the thermal parmater values using inverse modeling. In a second stage, we propose an indirect approach to estimate the different loss components based on the corrected thermal model from the first stage. Both stages are applied on a 4 kW axial flux yokeless and segmented armature (YASA) PM machine. In this machine, multiple temperature sensors have been inserted at different parts during the manufacturing. These positions were chosen independently of the parameters to estimate, *cfr.* non-collocated thermal sensors. Captured data at these non-collocated thermal sensors are then used to identify the thermal parameters and losses for specified load cycles.

Inverse thermal modeling techniques have been introduced in [22] to identify the lumped parameters in a simple thermal model. In [23], the iron losses were measured by solving the inverse heat source problem, and in [24] the losses sources in a lumped parameter thermal model of an induction motor were identified by inverse thermal modeling.

In contrast to [24] where the parameters of a simple lumped parameter thermal network were identified, this work introduces a high fidelity thermal finite element model including anisotropic thermal material properties as the forward model. The order of this model is then strongly reduced by applying a parametric model order reduction based on moment matching method in such a way that it becomes suitable in terms of calculation effort and time for the required many iterations in the inverse modeling step.

In Section II a short introduction to the used and proposed methods is given and in Section III we present the experimental setup and measurement procedure. In the subsequent Section IV we illustrate that an inverse thermal modeling approach is capable to identify uncertain thermal parameter values such as winding filling factors, thermal conductivity values and convection coefficients. Based on the thermal model exhibiting high fidelity due to the correction of the thermal parameter values of the actual machine, results are provided in a second stage on estimating the different loss components based on the non-collocated thermal measurements and the improved thermal model.

II. Methodology

A. Forward Finite Element Model

The aim of the forward model is to achieve high accuracy in geometric details and thermal material modeling. Therefore, a finite element thermal model is preferred over a lumped parameter thermal network.

To identify the thermal parameters using the inverse model, a full transient solution of the thermal problem needs to be calculated by solving

$$\rho C_{\mathrm{p}} \frac{\partial T}{\partial t} - \nabla \cdot (k \nabla T) = Q \tag{1}$$

in each of the material volumes. In this equation, ρ is the mass density, $\mathrm{C_p}$ the specific heat capacity, k the thermal conductivity and Q the power loss density in the material volume.

B. State-Space Representation

A large-scale parametrized time-invariant state-space model is extracted from the forward finite element model. The dynamic and measurement equations are

$$\frac{\mathrm{d}\mathbf{x}(t)}{\mathrm{d}t} = \mathbf{A}(\mathbf{p})\mathbf{x}(t) + \mathbf{B}(\mathbf{p})\mathbf{u}(t) \tag{2}$$

$$\mathbf{y}(t) = \mathbf{C}(\mathbf{p})\mathbf{x}(t) \tag{3}$$

respectively, where the state-space matrices $\mathbf{A}(\mathbf{p}) \in \mathbb{R}^{n\times n}$, $\mathbf{B}(\mathbf{p}) \in \mathbb{R}^{n\times m}$ and $\mathbf{C}(\mathbf{p}) \in \mathbb{R}^{q\times n}$ are implicitly dependent on a parameter vector $\mathbf{p} \in \mathbb{R}^d$.

In the thermal model, the states $\mathbf{x}$ correspond to the temperatures in the domains in the discrete elements of the mesh, the inputs $\mathbf{u}$ to the local power losses, and $\mathbf{y}$ being the temperatures in the points of interest where local measurements are obtained trough temperature sensors.

Since the numbers of sensors $\mathbf{y}$, *cfr.* subsection III-B, is much lower than the number of states $\mathbf{x}$, and moreover, the temperature sensors $\mathbf{y}$ are not a direct measurement of the power losses and can be located at a distance from the power loss components, *i.e.* non-collocated, an inverse model is required. The inverse model needs to estimate the thermal parameters of interest starting from temperature measurements by having correspondence between the model responses $\mathbf{y}(t)$ (simulated using model (6-7) and the temperature measurements $\mathbf{y}_{\mathrm{meas}}(t)$. This can be implemented by minimizing a least-squares objective function $\int_0^t \|\mathbf{y}_{\mathrm{meas}}(t) - \mathbf{y}(t)\|^2$. This objective function is evaluated in an iterative manner until a minimum squared error over time is found. Unfortunately, the states $\mathbf{x}$, and hence, the system matrices extracted from the finite element model are of large order (10^3 - 10^5), so multiple iterations result in prohibitively large computational effort. In order to decrease this effort, parametric model order reduction, more specifically moment matching method, was implemented.

C. Parametric Model Order Reduction

The aim of the model order reduction is to reduce the number of variables while preserving the input-output behavior of the original system, resulting in a reduced state-space system [25]

$$\frac{\mathrm{d}\tilde{\mathbf{x}}(t)}{\mathrm{d}t} = \tilde{\mathbf{A}}(\mathbf{p})\tilde{\mathbf{x}}(t) + \tilde{\mathbf{B}}(\mathbf{p})\mathbf{u}(t) \tag{4}$$

$$\mathbf{y}(t) = \tilde{\mathbf{C}}(\mathbf{p})\tilde{\mathbf{x}}(t) \tag{5}$$

where the state-space matrices $\tilde{\mathbf{A}}(\mathbf{p}) \in \mathbb{R}^{k\times k}$, $\tilde{\mathbf{B}}(\mathbf{p}) \in \mathbb{R}^{k\times m}$ and $\tilde{\mathbf{C}}(\mathbf{p}) \in \mathbb{R}^{q\times k}$, with $k \ll n$.

Since the considered system is parametrized and this relation must be conserved after order reduction, a parametric model order reduction based on moment matching method as proposed by [26], is applied.

Parameterization of the state-space matrices associated to the dynamic equation result in

$$\begin{aligned}\mathbf{A}(s_1, s_2, \ldots, s_{d-1}) = \mathbf{A_{s_1}} s_1 + \mathbf{A_{s_2}} s_2 + \ldots \\ + \mathbf{A_{s_{d-1}}} s_{d-1}\end{aligned} \tag{6}$$

$$\begin{aligned}\mathbf{B}(s_1, s_2, \ldots, s_{d-1}) = \mathbf{B_{s_1}} s_1 + \mathbf{B_{s_2}} s_2 + \ldots \\ + \mathbf{B_{s_{d-1}}} s_{d-1}\end{aligned} \tag{7}$$

with s being the $d-1$ moments of the state space matrix. Laplace transformation of (6) thus results in

$$[s\mathbf{1} - \mathbf{A}(s_1, s_2, \ldots, s_{d-1})]\mathbf{x} = \mathbf{B}(s_1, s_2, \ldots, s_{d-1})\mathbf{u} \tag{8}$$

Let us define $s_d = s$ and the right hand side of (12) is

$$\mathbf{E}(s_1, s_2, \ldots, s_{d-1}) = s_d\mathbf{1} - \mathbf{A}(s_1, s_2, \ldots, s_{d-1}) \tag{9}$$

resulting in the following Laplace domain representation for the states: $\mathbf{x}(s) = \mathbf{E}^{-1}(s)\mathbf{B}\mathbf{u}(s_d)$

Subsequently, the state $\mathbf{x}$ is expanded into a Taylor series at an expansion point $\mathbf{s^0} = (s_1^0, s_2^0, \ldots s_d^0)$

$$\begin{aligned}\mathbf{x(s)} =& \mathbf{x(s^0)} + \Delta\mathbf{x(s)}(\mathbf{s} - \mathbf{s^0}) \\ =& \mathbf{E}^{-1}(\mathbf{s^0})\mathbf{B}\mathbf{u}(s_d) \\ &+ [\mathbf{E}^{-1}(\mathbf{s}) - \mathbf{E}^{-1}(\mathbf{s^0})](\mathbf{s} - \mathbf{s^0})\mathbf{B}\mathbf{u}(s_d)\end{aligned} \tag{10}$$

Using the following definitions and notations

$$\tilde{\mathbf{E}} = \mathbf{E(s^0)} \tag{11}$$
$$\Delta s_i = s_i - s_i^0 \tag{12}$$
$$\mathbf{M_i} = \mathbf{E}^{-1}\mathbf{E_i} \tag{13}$$
$$\mathbf{B_M} = \tilde{\mathbf{E}}^{-1}\mathbf{B}(s_1, s_2, \ldots, s_{d-1}) \tag{14}$$

and the separation of the factor $\tilde{\mathbf{E}}^{-1}\mathbf{B}\mathbf{u}$ in equation (10) results in

$$\mathbf{x(s)} = [\mathbf{1} - (\Delta s_1\mathbf{M_1} + \ldots + \Delta s_d\mathbf{M_d})]^{-1}\tilde{\mathbf{E}}^{-1}\mathbf{B}\mathbf{u}(s_d) \tag{15}$$

The Neumann series expansion $(\mathbf{1} - \mathbf{A})^{-1} = \sum_k \mathbf{A}^k$ can be applied

$$\mathbf{x(s)} = \sum_{k=0}^{\infty}[\Delta s_1\mathbf{M_1} + \ldots + \Delta s_d\mathbf{M_d}]^k\mathbf{B_M}\mathbf{u}(s_d) \tag{16}$$

Expanding the summation results in

$$\begin{aligned}\mathbf{x(s)} = \mathbf{B_M}\mathbf{u} + [\Delta s_1\mathbf{M_1} + \ldots + \Delta s_d\mathbf{M_d}]\mathbf{B_M}\mathbf{u} \\ + [\Delta s_1\mathbf{M_1} + \ldots + \Delta s_d\mathbf{M_d}]^2\mathbf{B_M}\mathbf{u} \\ + \ldots\end{aligned} \tag{17}$$

where a recursive relation between the coefficients can be derived

$$\mathbf{G_0} = \mathbf{B_M} \tag{18}$$
$$\begin{aligned}\mathbf{G_1} &= [\Delta s_1\mathbf{M_1} + \ldots + \Delta s_d\mathbf{M_d}]\mathbf{B_M} \\ &= [\Delta s_1\mathbf{M_1} + \ldots + \Delta s_d\mathbf{M_d}]\mathbf{G_0}\end{aligned} \tag{19}$$
$$\begin{aligned}\mathbf{G_2} &= [\Delta s_1\mathbf{M_1} + \ldots + \Delta s_d\mathbf{M_d}]^2\mathbf{B_M} \\ &= [\Delta s_1\mathbf{M_1} + \ldots + \Delta s_d\mathbf{M_d}]\mathbf{G_1}\end{aligned} \tag{20}$$
$$\vdots$$

From this relation a vector sequence with the coefficient matrices is deduced

$$\mathbf{R_0} = \mathbf{B_M} \tag{21}$$
$$\mathbf{R_1} = [\mathbf{M_1R_0}, \mathbf{M_2R_0} \ldots, \mathbf{M_dR_0}] \tag{22}$$
$$\mathbf{R_2} = [\mathbf{M_1R_1}, \mathbf{M_2R_1} \ldots, \mathbf{M_dR_1}] \tag{23}$$
$$\vdots$$

The terms $\mathbf{R_j}$ are on one side the coefficient matrices of the parameters in a series expansion and on the other side the j^{th} order moment vectors. These vectors span a subspace $\mathcal{K}$

$$\mathcal{K} = \text{span}\{\mathbf{R_0}, \mathbf{R_1}, \ldots, \mathbf{R_j}\} \tag{24}$$

$\mathcal{K}$ is a Krylov subspace built, taking into consideration the coefficient matrices of the separate system parameters.

Finally, mapping of the original n-dimensional state-space into the reduced k-dimensional state-space occurs by means of multiplication with $\mathbf{V}$, an orthogonal projection matrix that satisfies $\mathbf{V}^{\mathrm{T}}\mathbf{V} = \mathbf{1_k}$:

$$\tilde{\mathbf{x}} = \mathbf{V}\mathbf{x} \tag{25}$$
$$\tilde{\mathbf{A}} = \mathbf{V}^{\mathrm{T}}\mathbf{A}\mathbf{V} \tag{26}$$
$$\tilde{\mathbf{B}} = \mathbf{V}^{\mathrm{T}}\mathbf{B} \tag{27}$$
$$\tilde{\mathbf{C}} = \mathbf{C}\mathbf{V} \tag{28}$$

III. Experimental Setup and Procedure

A. Axial Flux PM Machine

The thermal parameter identification and loss separation based on inverse thermal modeling will be illustrated on the stator of a yokeless and segmented armature (YASA) axial flux PM machine. In Fig. 1 a cross section of the 4 kW, 2500 rpm YASA-machine is illustrated, and the specifications are listed in Table I.

A characteristic property of the YASA-machine is its modular stator construction [27], [28]. In Fig. 2 a cross section view perpendicular to the shaft gives a view on the internal stator construction. Fifteen identical stator modules, each consisting of a laminated core, insulation and winding, are arranged into a stator housing. To improve the thermal heat flux from the modules to the stator outer surface, inward heat extraction fins are introduced [29]. The remaining narrow spaces between the different stator parts are filled with an epoxy resin [18].

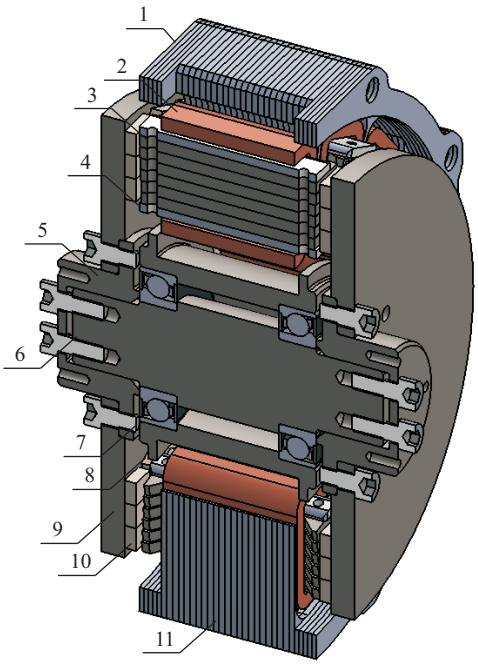

Fig. 1: Cross section view of the YASA AFPMSM. (1) laminated stator housing, (2) concentrated winding, (3) laminated core with six different profile shapes, (4) plastic end winding plate, (5) rotor adaptor, (6) shaft, (7) bearing, (8) bearing block, (9) rotor disc back-iron, (10) segmented permanent magnet, (11) inward heat extraction fin.

B. Non-Collocated Thermal Measurements

During the construction of the stator, several resistance temperature detectors (RTDs) have been integrated near the different stator parts. Their positions are indicated in Fig. 3. In the state space systems, the measurements in the different points correspond to the measurement vector $\mathbf{y}$ in equation (3). The positions of the RTDs are chosen such that they are located in different parts of the machine but, as mentioned previously, they are not a direct measurement of the thermal parameters to identify.

During the thermal measurements, the air gap surfaces of the stator are insulated by thermal covers (Fig. 4). To allow heat flux from the stator modules to the stator housing surface in radial direction, the stator outer surface remains uncovered. An external fan is faced towards the stator to allow sufficient cooling.

C. Measurement Procedure

The losses in the windings and the stator cores of the AFPMSM are generated by a Spitzenberger PAS10000 amplifier. By varying the applied voltage and frequency, different values for the iron and copper losses can be obtained. The ingoing power is continuously monitored by a Tektronix PA4000 power analyzer. To have uniform power losses over the different stator segments, all windings, independent of the phase, are put in series. This is possible because all wires of the individual stator modules are brought to a terminal block outside the AFPMSM stator, as can be seen in Fig. 4. To compensate for the temperature dependency of the electrical resistance of the windings, adjustments to the applied voltage are necessary to maintain constant power losses over time.

The RTDs are connected to an amplifying circuit using a four-wire connection. This limits the temperature-dependent

TABLE I: Key specifications of the YASA AFPMSM

Parameter	Value	Unit
Rated output power	4000	W
Rated speed	2500	rpm
Rated torque	15	Nm
Rated current	10	A
Pole number	16	-
Slot/tooth number	15	-
Outer diameter housing	195	mm
Outer diameter (active)	148	mm
Inner diameter (active)	100	mm
Axial length stator	61	mm
Total mass	9	kg
Magnet thickness	4	mm
Magnet width segments	18/21/24	mm
Magnets	NdFeB 40SH	-
Stator core material	M100-23P	-
Rotor back iron thickness	8	mm
Air gap length (variable)	$1 \leq 5$	mm
Slot width	11	mm

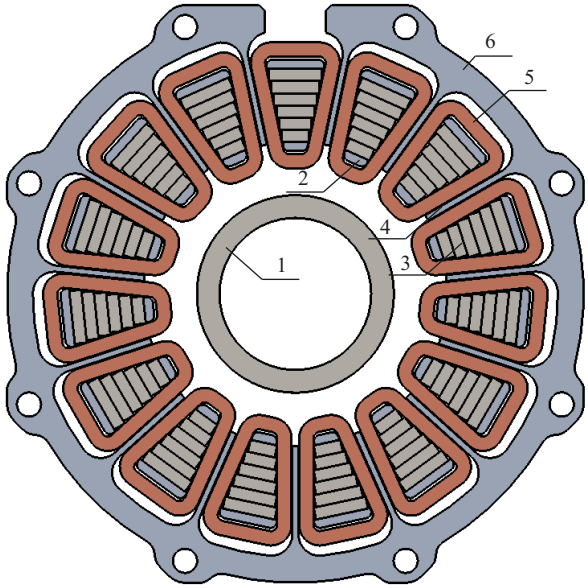

Fig. 2: Cross section view of the inward heat extraction fins in the YASA AFPMSM. (1) bearing block, (2) plastic end winding plate, (3) laminated core with six different profile shapes, (4) inward heat extraction fin, (5) concentrated winding, (6) laminated stator housing.

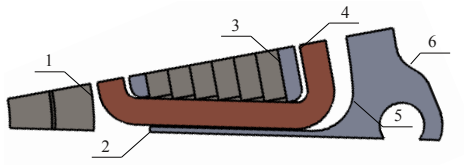

Fig. 3: Positions of the RTDs referred in the quarter tooth model.

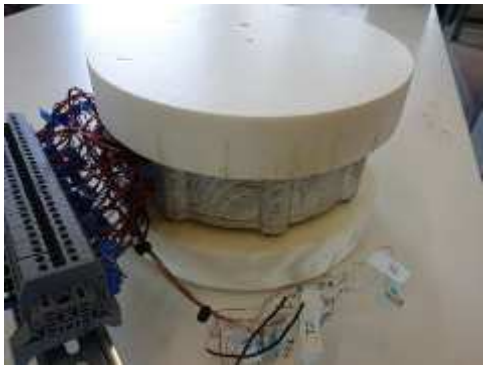

Fig. 4: Experimental validation set-up for the stator thermal model.

resistance of the RTD's wire connections. The temperatures captured by the RTDs are sampled synchronously every 5 seconds using a dSPACE 1104 platform.

IV. Experimental Results

In this Section the fidelity of the forward thermal model of the stator of an axial flux PM machine is improved by recovering the values of the uncertain thermal parameters based on actual experimental data of an axial flux PM machine. In a second stage, based on the improved thermal model and measurement data, iron and copper losses are separated.

A. Thermal Parameter Identification and Model Improvement

As mentioned in subsection III-A, the different stator modules and housing are assembled using epoxy potting techniques. As a consequence, the infiltration grade of the epoxy resin strongly influences the thermal properties of the stator. Bad infiltration grades result in air cavities reducing the overall thermal conductivity. The stator winding is most sensitive to the infiltration grade of the epoxy resin [15], [18]. A thermally good conduction is found in the direction parallel to the strands and a thermally bad conduction is found in the directions perpendicular to the strands.

Even in the forward finite element model, including geometry details up to the modeling of the individual laminations or winding strands is not feasible. Therefore, bulky volumes with homogenized material properties are used in this work. As a result, the thermal conductivity in equation (1) becomes a tensor instead of a scalar value. For an epoxy infiltrated winding, the equivalent thermal conductivity in the thermally good conduction direction is expressed by

$$k_{1,\mathrm{wi}} = f_{\mathrm{wi}} k_{\mathrm{cu}} + (1 - f_{\mathrm{wi}}) k_{\mathrm{ep}} \tag{29}$$

whereas in the thermally bad conduction direction, the equivalent thermal conductivity is expressed by the Hasihn and Shtrikman approximation [15]:

$$k_{2,\mathrm{wi}} = k_{\mathrm{ep}} \frac{(1 + f_{\mathrm{wi}}) k_{\mathrm{cu}} + f_{\mathrm{wi}} k_{\mathrm{ep}}}{(1 - f_{\mathrm{wi}}) k_{\mathrm{cu}} + (2 - f_{\mathrm{wi}}) k_{\mathrm{ep}}} \tag{30}$$

where k_{ep} is the thermal conductivity of the epoxy resin, k_{cu} the thermal conductivity of copper and f_{wi} is the winding filling factor.

Equivalently, the specific heat capacity and mass density are expressed as a function of the filling factor:

$$C_{\mathrm{p,wi}} = f_{\mathrm{wi}} C_{\mathrm{p,cu}} + (1 - f_{\mathrm{wi}}) C_{\mathrm{p,ep}} \tag{31}$$

$$\rho_{\mathrm{wi}} = f_{\mathrm{wi}} \rho_{\mathrm{cu}} + (1 - f_{\mathrm{wi}}) \rho_{\mathrm{ep}} \tag{32}$$

In Table II, the different material parameters and homogenized material properties are listed.

In Fig. 5 the geometry of the forward finite element model is presented. The epoxy resin material filling the empty space between the different parts is not shown. For thermal symmetry reasons, only one quarter of an equivalent stator module needs to be modeled [30]. The thermal symmetry is imposed by $\mathbf{n} \cdot (k \nabla T) = 0$ on the boundaries of the reduced geometry, except at the outer stator housing boundary. Here, convective heat transfer is expressed through

$$\mathbf{n}(k \nabla T) = h(T_{\mathrm{amb}} - T) \tag{33}$$

where T_{amb} is the ambient temperature.

The iron and copper losses are imposed uniformly over the core and winding, respectively. This assumption is acceptable for the core losses since the variable air gap results in a uniform magnetic flux density over the different lamination layers [31].

The validity of the material parameters is based on reference data. Nevertheless, some parameters might differ from these values. This is especially the case for the parameters of the epoxy resin. Here, the specific heat capacity is not specified in the datasheet. Its thermal conductivity might also be influenced by the infiltration grade and air inclusions within the resin. Relatively large amounts of air inclusions are expected in the prototype stator since no vacuum was applied during the infiltration process. Furthermore, as the stator in the measurement setup is only capable to evacuate heat by convection via the stator housing, this uncertain parameter needs to be determined as well. Inverse modeling will be engaged to characterize the above-mentioned uncertain parameter values such that the fidelity of the forward thermal model is increased. Therefore, the inverse modeling technique will be used to characterize these parameters, and consequently, improve the accuracy of the forward thermal model.

The aim of this subsection is to identify the parameter vector $\mathbf{p}$ in equation (2-3) consisting of the thermal conductivity k_{ep} and specific heat capacity $C_{\mathrm{p,ep}}$ of the epoxy compound and the convective heat transfer coefficient h at the stator housing, by means of inverse modeling.

To check the observability of the thermal parameter variations to the measured temperatures in the positions indicated in Fig. 3, a sensitivity analysis was performed. In this analysis, the winding losses are rated at 40 W, and the thermal

This article has been accepted for publication in a future issue of this journal, but has not been fully edited. Content may change prior to final publication. Citation information: DOI 10.1109/TIE.2018.2838089, IEEE Transactions on Industrial Electronics

TABLE II: Thermal parameters of the relevant materials used in the stator. The initial values used in the forward thermal model are notated in regular font, the ones determined though inverse modeling in *(italic)*.

	Bearing block	**Housing**		**Winding**		**Core**	
	C45	Epoxy	Aluminium	Epoxy	Copper	Epoxy	Steel
Fill factor		4	96	47	53	2	98
Mass density [kg/m^3]	7850	1540	2712	1540	8890	1540	7850
ρ_{eq}		2665		5730		7708	
Specific heat capacity [J/kg K]	480	600 *(1698)*	896	600 *(1698)*	385	600 *(1698)*	480
$C_{\mathrm{p,eq}}$		884 *(924)*		480 *(984)*		483 *(505)*	
Thermal conductivity [W/m K]	46	0.4 *(0.23)*	237	0.4 *(0.23)*	385	0.4 *(0.23)*	46
$k_{1,\mathrm{eq}}$		160 *(160)*		221 *(196)*		45 *(45)*	
$k_{2,\mathrm{eq}}$		18 *(11)*		1.5 *(0.7)*		25 *(17)*	

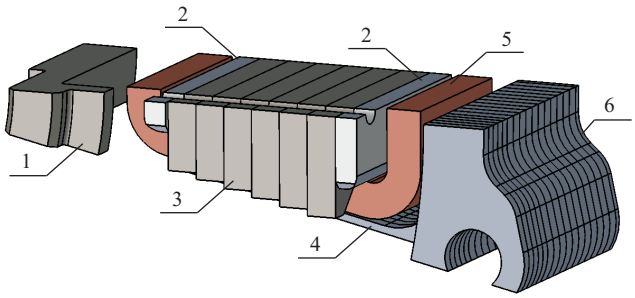

Fig. 5: Geometry modeled in the quarter of a stator module FEM, epoxy potting material is not shown. (1) bearing block, (2) plastic end winding plate, (3) laminated core with six different profile shapes, (4) inward heat extraction fin, (5) concentrated winding, (6) laminated stator housing.

parameters have the values indicated in Table II. A change in the value of the convective heat transfer coefficient h shows a good variation over its practical limits as indicated in Fig. 6c and mainly determines the steady-state temperatures. In contrast, as illustrated in Fig. 6b, the specific heat capacity $C_{\mathrm{p,ep}}$ value mainly influences the temperature transient, while the steady-state remains the same in each sensor. For both h and $C_{\mathrm{p,ep}}$ a sufficiently large variation is observed in all sensors. For the thermal conductivity of the epoxy resin k_{ep} in Fig. 6a, only the temperature sensors T3 and T4 show a detectable variation. Moreover the sensitivity is less visible for higher values of k_{ep}. This is inherent to the construction of the stator (Fig. 5): the thin layer of epoxy resin insulates the stator core and winding from the rest of the stator. Therefore, the highest variation is expected in the stator core (T3) and the stator winding (T4).

Fig.7 illustrates the implemented algorithm based on the forward model and inverse model earlier discussed. To safeguard accuracy of the reduced order model used in the inverse modeling step, a model convergence check was performed. In this way, the order of the model was reduced from 79331 in the high fidelity thermal finite element model to 119 in the state-space system equation (4).

The measurement data, which is the input of the inverse model, is generated by a specified input cycle. In this experiment the individual stator modules are all put in series and a specified DC-current is imposed by the power source. The DC-current was chosen to mitigate Eddy currents, of which the magnitude and location in the machine might be unpredictable. As a consequence, only resistive losses in the windings are present. During the experiment, 40W of copper loss in the stator windings was maintained over time, and was constantly monitored by a power-analyzer. The copper loss in the machine were kept constant until steady-state behavior was observed after about eight hours. The current was then powered off and the stator started to cool down. During the cooling process, data is still collected for four more hours. To enforce the convective heat transfer at the stator boundary surface, a external fan is faced towards te measurement setup.

Fig. 8 depicts the temperatures measured at the different sensor positions indicated in Fig. 3. A comparison with the simulation results from the forward model using the initial thermal parameters, presented in Fig. 9, shows some significant differences. The first major difference is the difference in steady-state temperature due to underestimating the thermal conductivity of the epoxy compound k_{ep} or the convective heat transfer coefficient h at the stator housing in the forward model. A second major difference is the transient in the heating and cooling phase. Temperatures in the forward model react much faster, which might be caused by an underestimation of the specific heat capacity $C_{\mathrm{p,ep}}$ of the epoxy compound.

Execution of the inverse modeling algorithm (see Fig. 7) results in a parameter set that approximates closer the actual values. In agreement with the comparison of the differences between measurements and forward model with the initial

This article has been accepted for publication in a future issue of this journal, but has not been fully edited. Content may change prior to final publication. Citation information: DOI 10.1109/TIE.2018.2838089, IEEE Transactions on Industrial Electronics

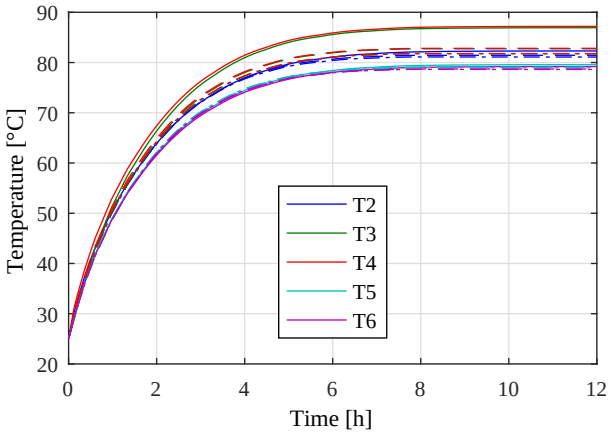

(a) Sensitivity of k_{ep}: 0.1 (–), 0.30 (- -), and 0.5 (-·) W/(m K)

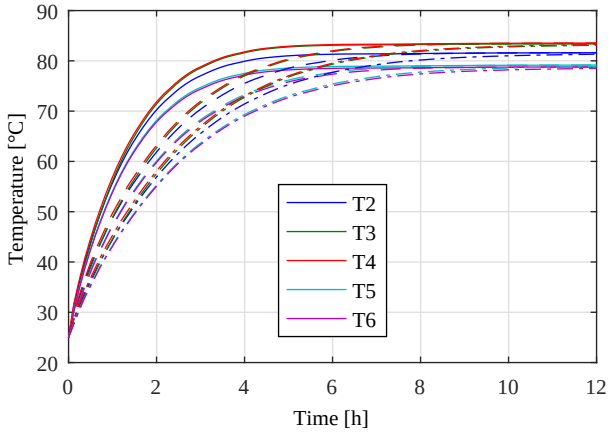

(b) Sensitivity of C_{ep}: 200 (–), 1100 (- -), and 2000 (-·) J/(kg K)

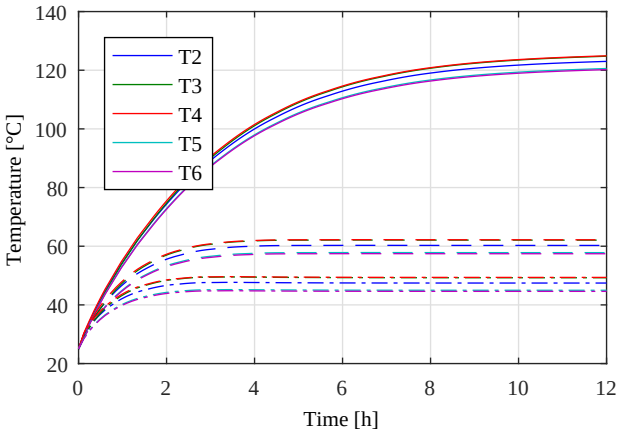

(c) Sensitivity of h: 10 (–), 30 (- -), and 50 (-·) W/(m^2 K)T

Fig. 6: Sensitivity analysis of the thermal parameters to the measured temperatures in the positions indicated in Fig. 3 using the forward model.

parameter set, the convective heat transfer coefficient h at the stator housing increases from 15 to 18.47 W/(m^2 K) and the specific heat capacity $C_{\mathrm{p,ep}}$ of the epoxy compound increases from 600 to 1698 J/(kg K). On the other hand, the thermal conductivity k_{ep} decreases from the initial 0.4 W/(m K) to

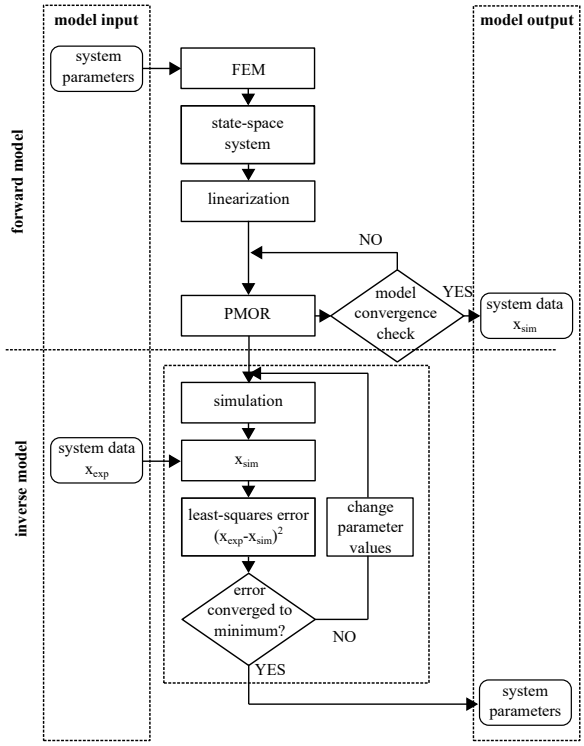

Fig. 7: Scheme of the inverse modeling algorithm.

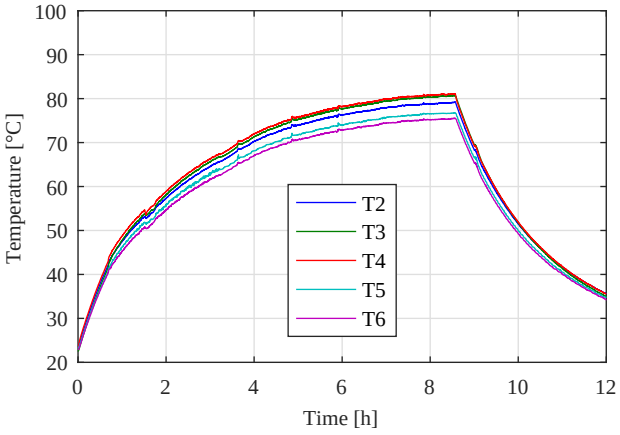

Fig. 8: Measured temperatures. Positions of the temperature sensors according to Fig. 3

0.23 W/(m K). As earlier discussed, this decrease might be the result of air inclusions and bad infiltration grades during the epoxy infiltration process.

Replacement of the initial parameter set by the one found through inverse thermal modeling, results in the simulated temperatures illustrated in Fig. 10. As can be noticed the steady-state temperatures as well as the temperature transients are in close agreement with the measurements. Temperature sensor T2 indicates a bigger difference with the sensors T3 and T4 than for the initial parameter set, and is in better agreement with the measurements. The smaller value for the thermal conductivity k_{ep} of the epoxy compound, insulates the core and winding (T3 and T4) better from the inward heat

This article has been accepted for publication in a future issue of this journal, but has not been fully edited. Content may change prior to final publication. Citation information: DOI 10.1109/TIE.2018.2838089, IEEE Transactions on Industrial Electronics

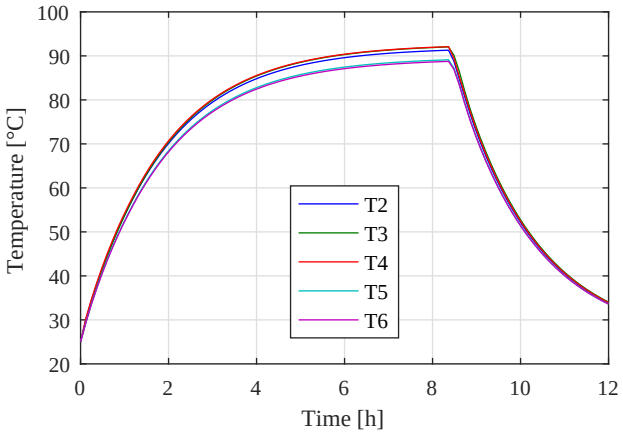

Fig. 9: Simulated temperatures calculated by the forward model using the initial set of parameters: k_{ep}=0.4 W/(m K), $C_{\mathrm{p,ep}}$=600 J/(kg K) and h=15 W/(m^2 K). Positions of the temperature sensors according to Fig. 3

extraction fin (T2). This results in a higher temperature drop as experimentally observed.

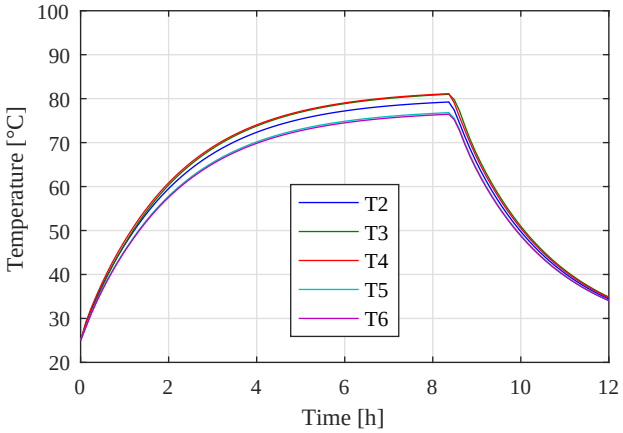

Fig. 10: Simulated temperatures calculated by the forward model using the improved set of parameters: k_{ep}=0.23 W/(m K), $C_{\mathrm{p,ep}}$=1698 J/(kg K) and h=18.47 W/(m^2 K). Positions of the temperature sensors according to Fig. 3

After the improvement of the indicated parameter set, the forward model is sufficiently accurate.

B. Iron and Copper Losses Separation

The corrected high fidelity thermal finite element model will be used in this paragraph through reduction to separate the iron and core losses in the stator of the axial flux PM machine. The same measurement setup *cfr.* Fig. 4 is used in this experiment. Different from the first experiment, an AC-current with a frequency of 200 Hz is imposed. This will result in both copper and iron losses. The total ingoing power is monitored with a power-analyzer and is maintained constant at 40 W.

Despite the high applied frequency of 200 Hz, the absence of the rotors in the measurement setup results in a particular low flux density of 0.2 T in the stator cores, and therefore, a very limited loss of about 6 W is imposed in the stator cores. This 6 W iron loss is based on finite element analysis of the magnetic flux density in the stator cores and material characterization based on Epstein frame measurements as described in [31].

Despite the core losses are only rated at 15% of the total loss, the sensitivity analysis in Fig.11 indicates that this variation is detectable using the temperature sensor T3 indicated in Fig. 3. This sensitivity analysis reveals that the sensor collocated to the stator core is required to separate the core losses from the other loss components.

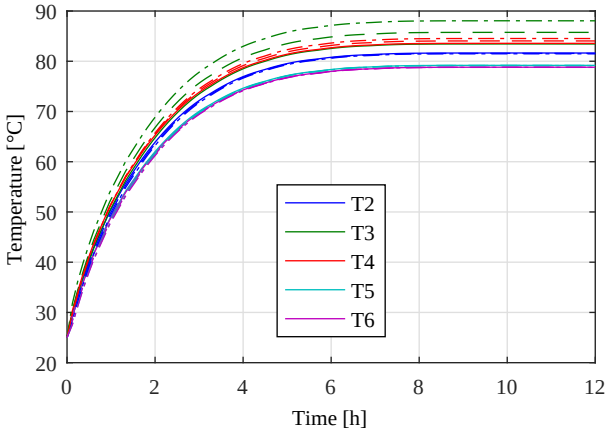

Fig. 11: Sensitivity analysis of the iron loss to the measured temperatures in the positions indicated in Fig. 3 using the forward model. A total loss of 40 W is assumed, simulations for 0 W (–), 20 W (- -), and 40 W (-·) iron loss.

In the algorithm presented in Fig. 7 the linearization process in the parameters is not required as the iron and copper losses are a direct input of the state-space model. In the optimization process the constraint is added that the sum of the losses should be less or equal to the total measured losses. This algorithm gives a best fit for 33.25 W copper losses in the winding and 6.75 W of iron losses in the stator cores.

The proposed approach accurately estimates the different loss components in the machine. It has to be noticed that the reduced order model of the forward model with the initial set of parameters was not capable to predict the loss component accurately. Also the order of the reduced model was increased from 119 to 605 as a result of the model convergence check in Fig. 7. This was a result of the increased number of inputs *i.e.* copper and iron losses instead of only copper losses. Moreover, according to Fig. 11, there is only limited sensitivity in one sensor (T3) while the thermal parameter identification state-space model showed an overall good sensitivity in all sensors. Therefore, it can be concluded that the loss separation requires a thermal model with higher accuracy compared to the one used to identify the thermal parameters.

V. Conclusion

In this work, a set of parameters of a high fidelity thermal finite element model of an axial flux PM machine was

improved by inverse thermal modeling via non-collocated thermal sensors integrated in the stator of the machine during the construction. To achieve a tractable inverse modeling step and associated reduction of the computational effort, a model order reduction based on moment matching performance was carried out.

Different uncertain thermal parameter values including the thermal conductivity k_{ep} and specific heat capacity $C_{\mathrm{p,ep}}$ of the epoxy compound and the convective heat transfer coefficient h at the stator housing, were in a first stage all accurately determined by the inverse thermal modeling. This resulted in an improved high fidelity thermal finite element model of an axial flux PM machine.

In a second stage, it was proven that a reduced model of the forward model with the improved set of thermal parameters was capable to separate the copper from the core losses in the stator of the axial flux PM machine. In this identification process, the recovered set of thermal parameter values was used and it was necessary to increase the order of the reduced model in order to obtain accurate loss estimations.

REFERENCES

[1] P. Lindh, M. G. Tehrani, T. Lindh, J.-H. Montonen, J. Pyrhönen, J. T. Sopanen, M. Niemelä, Y. Alexandrova, P. Immonen, L. Aarniovuori *et al.*, "Multidisciplinary design of a permanent-magnet traction motor for a hybrid bus taking the load cycle into account," *IEEE Transactions on Industrial Electronics*, vol. 63, no. 6, pp. 3397–3408, 2016.

[2] A. Di Gerlando, G. M. Foglia, M. F. Iacchetti, and R. Perini, "Thermal modeling for the design and check of an axial flux pm motor," in *Electrical Machines (ICEM), 2014 International Conference on*. IEEE, 2014, pp. 1441–1447.

[3] T. d. P. M. Bazzo, J. F. Kölzer, R. Carlson, F. Wurtz, and L. Gerbaud, "Multiphysics design optimization of a permanent magnet synchronous generator," *IEEE Transactions on Industrial Electronics*, vol. 64, no. 12, pp. 9815–9823, 2017.

[4] Z. Huang and J. Fang, "Multiphysics design and optimization of high-speed permanent-magnet electrical machines for air blower applications," *IEEE Transactions on Industrial Electronics*, vol. 63, no. 5, pp. 2766–2774, 2016.

[5] D. A. Howey, P. R. Childs, and A. S. Holmes, "Air-gap convection in rotating electrical machines," *IEEE Transactions on Industrial Electronics*, vol. 59, no. 3, pp. 1367–1375, 2012.

[6] R. Camilleri, P. Beard, D. A. Howey, and M. D. McCulloch, "Prediction and measurement of the heat transfer coefficient in a direct oil-cooled electrical machine with segmented stator," *IEEE Transactions on Industrial Electronics*, vol. 65, no. 1, pp. 94–102, 2018.

[7] S. Zhang, W. Li, J. Li, L. Wang, and X. Zhang, "Research on flow rule and thermal dissipation between the rotor poles of a fully air-cooled hydrogenerator," *IEEE Transactions on Industrial Electronics*, vol. 62, no. 6, pp. 3430–3437, 2015.

[8] W. Hua, H. Zhang, M. Cheng, J. Meng, and C. Hou, "An outer-rotor flux-switching permanent-magnet-machine with wedge-shaped magnets for in-wheel light traction," *IEEE Transactions on Industrial Electronics*, vol. 64, no. 1, pp. 69–80, 2017.

[9] H. Li, K. W. Klontz, V. E. Ferrell, and D. Barber, "Thermal models and electrical machine performance improvement using encapsulation material," *IEEE Transactions on Industry Applications*, vol. 53, no. 2, pp. 1063–1069, 2017.

[10] M. Polikarpova, P. Ponomarev, P. Lindh, I. Petrov, W. Jara, V. Naumanen, J. Tapia, and J. Pyrhönen, "Hybrid cooling method of axial-flux permanent-magnet machines for vehicle applications," *IEEE Transactions on Industrial Electronics*, vol. 62, no. 12, pp. 7382–7390, 2015.

[11] F. Marignetti, V. D. Colli, and Y. Coia, "Design of axial flux pm synchronous machines through 3-d coupled electromagnetic thermal and fluid-dynamical finite-element analysis," *IEEE Transactions on Industrial Electronics*, vol. 55, no. 10, pp. 3591–3601, 2008.

[12] Y. C. Chong, E. J. E. Subiabre, M. A. Mueller, J. Chick, D. A. Staton, and A. S. McDonald, "The ventilation effect on stator convective heat transfer of an axial-flux permanent-magnet machine," *IEEE Transactions on Industrial Electronics*, vol. 61, no. 8, pp. 4392–4403, 2014.

[13] A. Boglietti, A. Cavagnino, D. Staton, M. Shanel, M. Mueller, and C. Mejuto, "Evolution and modern approaches for thermal analysis of electrical machines," *IEEE Transactions on industrial electronics*, vol. 56, no. 3, pp. 871–882, 2009.

[14] D. Staton, A. Boglietti, and A. Cavagnino, "Solving the more difficult aspects of electric motor thermal analysis in small and medium size industrial induction motors," *IEEE Transactions on Energy Conversion*, vol. 20, no. 3, pp. 620–628, 2005.

[15] L. Siesing, A. Reinap, and M. Andersson, "Thermal properties on high fill factor electrical windings: Infiltrated vs non infiltrated," in *Electrical Machines (ICEM), 2014 International Conference on*. IEEE, 2014, pp. 2218–2223.

[16] X. Cai, M. Cheng, S. Zhu, and J. Zhang, "Thermal modeling of flux-switching permanent-magnet machines considering anisotropic conductivity and thermal contact resistance," *IEEE Transactions on Industrial Electronics*, vol. 63, no. 6, pp. 3355–3365, 2016.

[17] A. Boglietti, A. Cavagnino, M. Parvis, and A. Vallan, "Evaluation of radiation thermal resistances in industrial motors," *IEEE Transactions on Industry Applications*, vol. 42, no. 3, pp. 688–693, 2006.

[18] S. Nategh, A. Krings, O. Wallmark, and M. Leksell, "Evaluation of impregnation materials for thermal management of liquid-cooled electric machines," *IEEE Transactions on Industrial Electronics*, vol. 61, no. 11, pp. 5956–5965, 2014.

[19] P. Rasilo, U. Aydin, T. P. Holopainen, and A. Arkkio, "Analysis of iron losses on the cutting edges of induction motor core laminations," in *Electrical Machines (ICEM), 2016 XXII International Conference on*. IEEE, 2016, pp. 1312–1317.

[20] W. Jara, P. Lindh, J. A. Tapia, I. Petrov, A.-K. Repo, and J. Pyrhönen, "Rotor eddy-current losses reduction in an axial flux permanent-magnet machine," *IEEE Transactions on Industrial Electronics*, vol. 63, no. 8, pp. 4729–4737, 2016.

[21] G. Heins, D. M. Ionel, D. Patterson, S. Stretz, and M. Thiele, "Combined experimental and numerical method for loss separation in permanent-magnet brushless machines," *IEEE Transactions on Industry Applications*, vol. 52, no. 2, pp. 1405–1412, 2016.

[22] G. G. Guemo, P. Chantrenne, and J. Jac, "Parameter identification of a lumped parameter thermal model for a permanent magnet synchronous machine," in *Electric Machines & Drives Conference (IEMDC), 2013 IEEE International*. IEEE, 2013, pp. 1316–1320.

[23] L. Perkkiö, "Iron loss measurement as inverse heat source problem," in *Electromagnetic Field Computation (CEFC), 2016 IEEE Conference on*. IEEE, 2016, pp. 1–1.

[24] D. G. Nair and A. Arkkio, "Inverse thermal modeling to determine power losses in induction motor," *IEEE Transactions on Magnetics*, vol. 53, no. 6, pp. 1–4, 2017.

[25] W. H. Schilders, H. A. Van der Vorst, and J. Rommes, *Model order reduction: theory, research aspects and applications*. Springer, 2008, vol. 13.

[26] L. Feng, "Parametric model order reduction."

[27] B. Zhang, T. Seidler, R. Dierken, and M. Doppelbauer, "Development of a yokeless and segmented armature axial flux machine," *IEEE Transactions on Industrial Electronics*, vol. 63, no. 4, pp. 2062–2071, 2016.

[28] A. Di Gerlando, G. M. Foglia, M. F. Iacchetti, and R. Perini, "Parasitic currents in stray paths of some topologies of yasa afpm machines: Trend with machine size," *IEEE Transactions on Industrial Electronics*, vol. 63, no. 5, pp. 2746–2756, 2016.

[29] H. Vansompel, A. Hemeida, and P. Sergeant, "Stator heat extraction system for axial flux yokeless and segmented armature machines," in *Electric Machines and Drives Conference (IEMDC), 2017 IEEE International*. IEEE, 2017, pp. 1–7.

[30] P. Lindh, I. Petrov, J. Pyrhonen, M. Satrustegui, M. Martinez-Iturralde, A. Jaatinen-Varri, and A. Gronman, "Direct liquid cooling method verified with an axial-flux permanent-magnet traction machine prototype," *IEEE Transactions on Industrial Electronics*, 2017.

[31] H. Vansompel, P. Sergeant, L. Dupré, and A. Van den Bossche, "Axial-flux pm machines with variable air gap," *IEEE Transactions on Industrial Electronics*, vol. 61, no. 2, pp. 730–737, 2014.

Hendrik Vansompel was born in Belgium in 1986. He received the master's and Ph.D. degrees in electromechanical engineering from Ghent University, Ghent, Belgium, in 2009 and 2013, respectively.

He is currently a Postdoctoral Research Assistant with the Department of Electrical Energy, Metals, Mechanical Constructions and Systems, Ghent University. His research interests include the design and control of electrical drives.

Anna Yarantseva was born in Novosibirsk, Russia in 1992. She received the M.Sc. degree in control engineering and automation from Ghent University, Ghent, Belgium, in 2017. Her research interest includes thermal modeling applied to electrical drives and control-system theory.

Peter Sergeant received the M.Sc. degree in electromechanical engineering and the Ph.D. degree in engineering sciences from Ghent University, Ghent, Belgium, in 2001 and 2006, respectively. In 2001, he became a Researcher with the Electrical Energy Laboratory, Ghent University. He became a Postdoctoral Researcher at Ghent University in 2006 (Postdoctoral Fellow of the Research Foundation?Flanders) and at Ghent University College in 2008. Since 2012, he has been Associate Professor with Ghent University. His current research interests include numerical methods in combination with optimization techniques to design nonlinear electromagnetic systems, in particular, electrical machines for sustainable energy applications.

Guillaume Crevecoeur (°1981) received the MSc and the PhD degree in Engineering Physics from Ghent University in 2004 and 2009, respectively. In 2004 he joined the Department of Electrical Energy, Metals, Mechanical Constructions, and Systems as doctoral student and in 2009 he became a postdoctoral fellow of the Research Foundation Flanders (FWO-Flanders). In the winter 2011 he was a visiting researcher at the Technical University Ilmenau and the Physikalische Technische Bundesanstalt, Berlin, Germany. In 2014 he was appointed Associate Professor at the Faculty of Engineering and Architecture of Ghent University. He is furthermore an affiliate member of Flanders Make, the strategic research center for the manufacturing industry. His research interests are the modeling, optimization and control of dynamical systems including foundational work on model-based optimization algorithms, inverse problems and nonlinear optimal control with strategic research on electromechanical and biomedical applications.